ChemCatChem

Research Article
doi.org/10.1002/cctc.202402142

Chemistry Europe
European Chemical Societies Publishing

www.chemcatchem.org

Improving CO_2 Photoconversion by Layered Materials: Boosted Optoelectronic Performance and Catalytic Activity of g-C_3N_4 by Ultrasound Exfoliation

Matteo Tommasi,[a] Ehsan Abbasi,[a] Md. Imteyaz Alam,[b] Daniele Marinotto,[c] Ilenia Rossetti,*[a, b, c] and Gianguido Ramis[d, e]

This paper is dedicated to the memory of Prof. Lucio Forni, formerly professor at Università degli Studi di Milano, who passed away at the end of December 2022. I. Rossetti and G. Ramis, as students and colleagues, gratefully remember all the teachings and the moments spent together.

Exfoliation of graphitic carbon nitride g-C3N4 by means of ultrasound (US) treatment at varying input power is investigated. Exfoliation of g-C3N4 displays a strong dependence of US input power, with a slightly enhanced bandgap (2.8 eV), but most of all increased lifetime of photogenerated electrons, as observed through diffuse reflectance spectroscopy (DRS) and spectrofluorimetry data. Among all applied power (varied between 30 and 120 W), 120 W sufficiently exfoliated and tuned physicochemical properties of g-C3N4. Compared to bulk as prepared sample, exfoliated g-C3N4 exhibited improvement in photo-induced charge carrier transfer and separation, resulting in higher photocatalytic efficiencies. FE-SEM and TEM images of both bulk and exfoliated g-C3N4 show the effect of the exfoliation power on the nanosheet, pseudo-lamellar structure. A change in US input power correlates well with amonotonous variation of the bandgap, of the charges lifetime of the materials and, most importantly, of the catalytic performance determined through an innovative high-pressure reactor in solid–liquid–gas phase. The catalytic results demonstrate this material as an efficient photocatalyst to obtain high yield of formic acid with net productivities ranging from ~5100 to ~8200 mmol/kg_{cat} h at 80 °C in water, which is among the highest reported in the literature.

1. Introduction

Climate change due to anthropogenic CO_2 emission from fossil fuel consumption and increased chemical demands with rising population has called for an alternative solution to alleviate the energy crisis and mitigate CO_2 input into the environment.[1] To address such issues, extensive CO_2 valorization and net zero-CO_2 technologies are crucial. In this context, solar-driven CO_2 reduction to valuable chemicals and fuels has inspired growing interests[2] because of (i) abundance of inexpensive sunlight, (ii) possible utilization of anthropogenic CO_2, and (iii) conceivable renewable products such as methane, methanol, formaldehyde, formic acid (FA), and hydrogen. Owing to hydrogen storage ability, ease of transportation, and possible transformation/derivatization into various products, FA production is one of the most attracting.[3–6] As its current production is relying on nonrenewable fossil-derived CO,[7] a renewable source with advancement in technology is highly desirable. Moreover, global annual production of formic acid (0.74 million tons in 2021)[8] is comparatively lower than the demand, even far less than the current CO_2 emission scale (36.3 billion tons in 2021).[9] With an aim to develop technology from clean, renewable, and cheap energy source, Avantium initiated formic acid production from CO_2.[10] According to 2021 report by Lux research, more than 80 firms are operational in developing new approaches for CO_2 utilization, which accounts less than $1 billion current global market.[11,12] Instead, it is expected to reach $70 billion market value by 2030 that will increase further to $550 billion by next 10 years in 2040. Thus, it would be helpful to develop a simple, sustainable, and scalable process of making FA from CO_2.

Nevertheless, reduction of CO_2 to formic acid is challenging due to chemical inertness (C—O bond energy of 799 kJ/mole), high thermodynamic stability ($\Delta H_f° = -393.5$ kJ/mol at 25 °C), large kinetic barriers, and low selectivity to FA. Success can be achieved through tuning temperature, pressure, reactant/product concentrations, and catalysts applied.

[a] M. Tommasi, E. Abbasi, I. Rossetti
Chemical Plants and Industrial Chemistry Group, Dip. Chimica, Università degli Studi di Milano, via C. Golgi 19, Milan 20133, Italy
E-mail: ilenia.rossetti@unimi.it

[b] M. I. Alam, I. Rossetti
INSTM Unit Milano-Università, via C. Golgi 19, Milan 20133, Italy

[c] D. Marinotto, I. Rossetti
Institute of Chemical Sciences and Technologies "Giulio Natta" (SCITEC), CNR, via Golgi 19, Milano 20133, Italy

[d] G. Ramis
Dip. Ing. Chimica, Civile ed Ambientale, Università degli Studi di Genova, via all'Opera Pia 15A, Genoa 16145, Italy

[e] G. Ramis
INSTM Unit Genova, via all'Opera Pia 15A, Genoa 16145, Italy

Supporting information for this article is available on the WWW under https://doi.org/10.1002/cctc.202402142

In this regard, use of semiconducting materials plus irradiation is promising. Introduction of a base can further shift thermodynamic equilibrium toward product side or at least increase the amount of CO_2 absorbed in the reaction medium.[13,14] Consequently, significant FA productivity with TONs $> 8 \times 10^4$ and TOFs $2 \times 1\,10^4$[15] has been reported in basic ionic liquid mediated reaction using Ru-based organometallic catalyst. An inorganic photocatalyst-enzyme system produced 16.75 10^3 μM formic acid in 9 h under 2 bar solution pressure.[16] To minimize waste generation from base and reduce production cost (e.g., ionic liquid and noble metals), CO_2 hydrogenation under UV irradiation in varying solvents resulted in 8.8 μmol FA with 141 TON and ~17 μmol FA in presence of Ru catalyst.[17,18] Furthermore, Mo—Bi—Cd exhibited 72% faradic efficiency with 208 μmol/g h FA in presence of ionic liquid.[19] An improvement to 725 μmol/g FA in 24 h was noticed, whereas Fe-based metal–organic framework catalyst was applied in a mixture of DMF and triethanolamine.[20] More recently, 2D porphyrin based covalent organic framework (COF) thin film was prepared by interfacial synthesis and tested to form 334.1 μmol FA.[21]

To make the process economic and environmentally friendly, there is a need to replace high boiling organic solvents with greener alternatives like water and to design a low-cost catalyst (preferably metals-free) in a simpler way with enhanced photocatalytic properties. Furthermore, the use of heterogeneous semiconductors is mandatory for scale up and continuous operation.

CO_2 photoreduction takes place when the bottom of conduction band of a photocatalyst is more negative than the CO_2 reduction potentials and the top of valence band must locate at more positive potential than the hole scavenger (HS) oxidation potential. In this regard, semiconducting materials are promising. Ability to harvest visible light and adsorb CO_2 make a material even more desirable, albeit activity of such materials is dependent on the dynamic behavior of charge carriers such as their trapping, recombination, and transfer.[2] This in turn depends on structure, size, and interface of the nanomaterials,[22] possibly leading to inefficient photoconversion and low products selectivity. Recent literature on photocatalytic applications is dominated by TiO_2.[23] However, the relatively wide bandgap (~3.2 eV) and low quantum efficiency with low visible light utilization (~4% of total light, i.e., UV light) limits its application. Besides, separation efficiency of photogenerated electron-hole pairs is insufficiently low, causing only a few of them to reach the catalyst–liquid interface to participate in photocatalytic reaction.[24,25]

Interestingly, g-C_3N_4 possesses moderate bandgap of 2.7 eV with high conduction band potential, which can facilitate CO_2 activation in a wide spectral range of sunlight (~43% of solar spectrum or visible light). Low cost, metal free composition, simple preparation, high thermal stability (600 °C), and many promising properties (unique structural, optoelectronic, and physicochemical properties) of g-C_3N_4.[26–29] made it a superior choice with respect to titania, which is only active under UV radiation. A stimulating study by Gao et al. also observed reduced barrier while impregnating Pt/Pd on g-C_3N_4.[30]

Unfortunately, the photocatalytic activity of g-C_3N_4 is unsatisfactory due to rapid charge recombination caused by stacking of the layers, that is, short lifetime of photogenerated electrons and holes,[31] and the low surface area limits the adsorption of reactants. Luckily, the typical structure of g-C_3N_4 facilitates the development of various effective approaches to address these inadequacies. Specifically, weak van der Waals interaction within layers allows exfoliation to reduce thickness and increase surface area for enhanced charge separation and transportation.[32,33] Therefore, different exfoliation methods may be applied to improve properties and performance of these materials. An overview of the different exfoliation methods to synthetize g-C_3N_4 for photoreduction, with a focus on advantages and potential limitations of the methods, is reported in Table 1.

In this paper, we have investigated an innovative US-assisted treatment for the exfoliation of g-C_3N_4 and, in turn, evaluate the effect of US exfoliation on the properties and overall quality of the final material (exfoliated g-C_3N_4). Furthermore, we demonstrated improved optoelectronic properties of g-C_3N_4 when increasing the input power of ultrasonic treatment from 30 to 120 W. The photocatalytic efficiency directly correlates with the resulting materials properties and with input power in ultrasound-induced exfoliation. Although this study is restricted to this specific material and application, this exfoliation technique can be extended to other 2D-layered materials for obtaining high quality finely-layered materials and to tune their properties for wide range of applications. An overview of the ultrasonic methods applied to exfoliate different 2D materials, highlighting their potential advantages and limitations, is reported in Table 2. The photocatalytic performance of the prepared materials is reported under nonconventional conditions (up to 20 bar and up to 80 °C), anticipating one of the highest productivities reported for the photoreduction of CO_2 to FA (ca. 10 mol/kg_{cat} h).

2. Experimental Section

2.1. Catalysts Preparation

Formic acid, melamine, and sodium sulfite were purchased from Sigma-Aldrich. Unless stated differently, all the materials were used without further treatment.

The g-C_3N_4 bulk catalyst was prepared in a tubular furnace by thermal condensation of melamine over the continuous flow of air (30 mL/min) at desired temperature (>525 °C) for 4 h. In a typical procedure, 5 g melamine was weighed into a quartz cuvette. The cuvette was then placed in a tubular furnace (Carbolite, UK) connected with the pure air line (30 mL/min), and it was allowed to heat at a rate of 1 °C/min to the target temperature (550 or 600 °C) and then kept for 4 h. After cooling down the furnace to ambient temperature (1 °C/min), the sample was removed and crushed to powder. The resulting yellowish powder (g-C_3N_4 bulk) was then exfoliated by US treatment at different input power for a fixed time of 3 h (5 h with 3 s on and 2 s off). It is to note that the instrument does not directly allow to adjust power or time of treatment. Hence, energy was first set and then power was accordingly calculated. In our experiments, we have applied energy in the range of 0.32–1.3 MJ, which corresponds (at fixed time) to an input power of 30–120 W, by

Table 1. Comprehensive summary of different exfoliation methods for g-C_3N_4 for photoreduction with advantages and potential limitations of the methods.

Entry	Exfoliation Technique	Key Process Details	Photoreduction Performance	Advantages	Limitations	Reference
1	Thermal exfoliation	High temperature calcination (600 °C) at ambient air for 2 h	-Increased surface area -Enhanced charge separation	-Relatively simple and effective -Can produce porous structure, resulting in increased surface area -Promotes exfoliation of the material due to simultaneous layer-by-layer thermal oxidation and layer splitting -Introduced structural and chemical defects (oxygen functionalities in g-C_3N_4, changing electronic properties of materials	-Requires high energy input -May lead to structural damage due to uncontrolled heating -Difficult to control layer thickness -Reduced effect on the bandgap energy of the prepared photocatalyst	[34–36]
2	Chemical exfoliation	Acid treatment (H_2SO_4/HNO_3 24 h)	Overoxidation leads to structural defects; reduced charge efficiency	-Acids or bases, disrupts van der Waals forces, yielding high surface area with increased active sites -Introduces oxygenated functional groups -Widen up the already large bandgap and improves visible light absorption	-Use of chemicals can generate hazardous waste -Can be complex and expensive -Possible structural damage, requires postwashing	[37–40]
3	Ultrasonic exfoliation	Sonication in water	Good visible light harvesting	-Can be scaled -Less harsh method compared to chemical exfoliation, minimizing potential damage to the g-C_3N_4 structure -It can be performed in different solvents, allowing for flexibility in processing and subsequent applications -Allows for the potential to tailor the surface properties of the resulting g-C_3N_4 by using various solvents	-Requires prolonged sonication time -Although milder than chemical exfoliation, prolonged or high-intensity sonication can still introduce defects into the g-C_3N_4 structure	[41]
4	Mechanical exfoliation	Ball milling or shear force grinding (dry/wet)	Oxygen functionalities in g-C_3N_4, changing electronic properties of materials, leading improved photoreactivity	-Minimal chemical waste -Preserves crystallinity -Introduced structural and chemical defects -Widen up the already large bandgap	-The high shear forces involved can introduce structural defects and damage the g-C_3N_4 lattice -It is challenging to control the size and uniformity of the exfoliated nanosheets -Possibility of impurities from the milling equipment being introduced into the final product	[42]

keeping 3 h sonication time constant. Materials calcined at 550 and 600 °C with sonication power 120 W are labelled as GC550-120 W and GC600-120 W, respectively. Similar notations were followed for other samples exfoliated at variable power.

2.2. Photocatalytic Tests of g-C_3N_4 for Photoreduction of CO_2

Photocatalytic studies were performed according to our previous reports,[45–47] in a specially designed stainless steel high-pressure photoreactor surrounded by a jacket for circulating water with 1.3 L available internal volume. The reactor is equipped with a pressure transducer, a double-walled thermostatic system, a thermocouple (to measure internal temperature), and a long quartz candle containing the light source, that is, a 125 W medium pressure Hg-vapor lamp (wavelength 254–364 nm). A scheme is reported in Figure S0.

In our typical testing procedure, g-C_3N_4 (0.031 g/L) along with 1.3 L sodium sulfite solution (1.66 g/L, as a hole scavenger, HS) in distilled water was loaded, and a magnetic bar was placed for continuous stirring of the mixture. Then, the reactor was closed and the

Table 2. Literature examples of ultrasonic methods applied to exfoliate different 2D materials, summarizing their potential advantages and limitations.

Entry	Material	Process Details	Advantages	Limitations	Performance/Outcome	Reference
1	Graphene	Sonication in ethanol at 37–80 kHz, low power	Produces monolayer/few layers graphene flakes -Cost effective -Low defect density	-Requires precise frequency control -Limited scalability	77% of flakes with <3 layers; lateral size ~13 μm	[41]
2	TiB_2	Probe sonication in water	-Green, single step process -Scalable -High aspect ratio nanosheets	-Prolonged treatment reduces lateral dimensions -Requires centrifugation	Thickness reduced to 21 nm; lateral dimensions up to 5 μm (input power dependent)	[43]
3	h-BN	Probe sonication in DI water at 60 °C	-Eco-friendly -Stable dispersion	-Requires centrifugation -Limited lateral size	Few layer h-BN nanosheets with stable dispersion for > one month	[44]
4	MoS_2	Bath sonication in DI water at 60°C	-Surfactant free -High stability	Requires long processing time	Few-layer MoS_2 nanosheets with stable dispersions	[44]

solution was then outgassed with CO_2 at a constant flow of 15 mL min^{-1} at 13 bar pressure with the objective to remove all residual oxygen from the reactor. The solution was saturated with CO_2 by applying a static pressure of 7–20 bar at ambient temperature and left overnight to assure saturation. Prior starting the reaction, the resulting pressure was measured and noted as reference. The reactor was allowed to heat at the desired reaction temperature under continuous stirring. Formic acid was measured through HPLC (Jasco, composed of HPLC pump mod. PU-4180, UV–vis detector mod. 4070 and RI detector mod. 4030), whereas the gaseous molecules were analyzed in GC (Agilent, mod. 7890). The consumption of the sulfite hole scavenger was done by iodometric titration.

2.3. Catalyst Characterization

X-ray diffraction (XRD) analyses were performed with Rigaku Miniflex-600 horizontal-scan powder diffractometer (Tokyo, Japan) using Cu Kα radiation with a graphite monochromator on the diffracted beam. Crystallite size was calculated according to the Scherrer Equation (1):

$$D = \frac{K\lambda}{\beta\cos\theta} \tag{1}$$

where D is the crystal size, λ is the X-ray wavelength (0.154 nm with Cu Kα generator), K is the shape factor (0.9), β is the width at half-maximum of the peak (i.e., FWHM), and θ is the Bragg angle.

Surface area and porosity were determined by collecting N_2 adsorption–desorption data at −196 °C. The isotherms were collected using a Micromeritics ASAP 2020 instrument. Before the analysis, pretreatment of the sample was performed under vacuum at 150 °C for 4 h to remove any contaminants or traces of water present in the catalysts. The data obtained were processed following the Brunauer–Emmett–Teller (BET), Barrett–Joyner–Halenda (BJH), and t plot analysis methods.[48]

Elemental analysis has been performed with a PerkinElmer 2400 Series II CHNS/O elemental analysis instrument.

Scanning electron microscopy (SEM) images and energy-dispersive X-ray analysis (EDX) were obtained using a JSM-7900F Schottky field emission scanning electron microscope (JEOL, Tokyo, Japan), operating at an accelerating potential of 20 kV. The 3D analysis of the surface has been elaborated by using the Image J software.

Transmission electron microscopy (TEM) images and energy-dispersive X-ray analysis (EDS) were collected using a FEI Tecnai G2 F20 transmission electron microscope operating at an accelerating potential of 200 kV.

2.4. Optical Characterization

Diffuse reflectance (DR) UV–vis spectra of samples were recorded on a Shimadzu UV-3600 Plus (Kyoto, Japan), using an integrating sphere and $BaSO_4$ as reference standard. Measurements were recorded between 190 and 700 nm with 1 nm intervals and spectral bandwidth of 20 nm. The results were processed according to the Kubelka–Munk elaboration and with Equations (2) and (3), using the reflectance spectra as input data.

$$(F(R)\,h\nu)^{\frac{1}{n}} = B\left(h\nu - E_g\right) \tag{2}$$

where h represents the Planck constant, ν the light frequency, n is a coefficient that is considered equal to $\frac{1}{2}$ when referring to the direct transition and equal to 2 when referred to the indirect transition,[49,50] E_g is the bandgap expressed in eV, and B represents the absorption constant corrected for a proportional factor between $F(R)$ and the molar extinction coefficient.

$$F(R_\infty) = \frac{(1-R_\infty)^2}{2R_\infty} \tag{3}$$

Tauc plot method was applied to evaluate bandgap energy (E_g) of the samples. The calculated $(F(R)h\nu)^{1/r}$ values (with $r = 2$ or $\frac{1}{2}$ for direct and indirect bandgap) were plotted against $h\nu$ to obtain the bandgap of each sample.[51] Due to the strong absorption of the materials, the g-C_3N_4 was mixed with $BaSO_4$ (50 wt%) with a mortar and pestle prior to recording the spectra to prevent saturation in the case of samples absorbing strongly. Therefore, the shape of the curves was not affected by the blending, but the absolute value of reflectance cannot be compared.

The photoluminescence measurements of the powder samples were studied at room temperature. Absolute photoluminescence quantum yield, Φ, was determined through a C11347 Quantaurus spectrometer (Hamamatsu Photonics K.K) equipped with a 150 W Xenon lamp, an integrating sphere, and a multichannel detector.

Steady state and time-resolved fluorescence data were obtained using a FLS980 spectrofluorometer (Edinburgh Instrument Ltd). Emission spectra were corrected for background intensity and quantum efficiency of the photomultiplier tube, whereas excitation spectra were corrected for intensity fluctuations of a 450 W Xenon lamp. Time-resolved fluorescence decay measurements were performed by time-correlated single photon counting technique

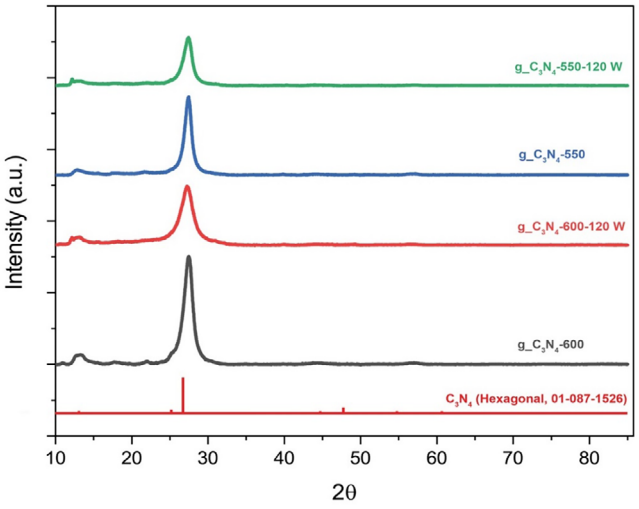

Figure 1. XRD patterns of g-C_3N_4 synthesized at 550 and 600 °C, including bulk and exfoliated samples at US-power 120 W, with corresponding ICDD data.

using an Edinburgh picosecond pulsed laser (emitted wavelength 374 nm).

3. Results and Discussion

3.1. Materials Characterization

Carbon nitride is an important material that can harvest sunlight in the visible range and has demonstrated activity to produce important products from CO_2. A change in catalyst preparation methods such as types of precursors, synthesis temperature, and exfoliation approaches can influence catalytic properties. Indeed, variation in thermal condensation of precursor molecules is crucial in adjusting electronic and optical properties of g-C_3N_4.[28] An increase in US power can lead to better material homogenization and reduction in particle size, which can improve the surface, optical, and electrical properties. However, if the US power is too high, it may damage the material and results in deterioration of such properties. Considering this, we have determined to tune the US power to optimize its effect on the properties of the material.

Another possible reason for enhanced properties in US-exfoliated g-C_3N_4 is ascribed to the force induced by ultrasound and the interaction with solvent molecules. Previous studies on exfoliation of layered g-C_3N_4 has focused on role of solvents,[32] sonication duration, frequency, and type of materials. However, studies on input US power for exfoliation are missing and this study aims to fill this gap.

With this in mind, starting from previous protocols,[52] we have modified g-C_3N_4 preparation method by thermal condensation of melamine at two different temperatures, 550 and 600 °C, under air flow. The XRD patterns of powder g-C_3N_4 are portrayed in Figure 1. It illustrates the characteristic interlayer stacking reflections of conjugated aromatic system at ~27.7° and ~13.1°, which correspond to (002) and (100) crystal planes, respectively.[53,54] The observed low intensity peak at 13.1° was attributed to the in-plane structural packing motif. As illustrated in Figure 1, there is a significant decrement in the intensity of (002) peak after exfoliation, which is remarkable to demonstrate successful exfoliation of layered carbon nitride.[54] Moreover, the two consistent reflections with exfoliated g-C_3N_4 suggest that the nanosheets essentially have the same crystal structure as their parent bulk counterpart, that is, the layers of g-C_3N_4 phase. Such diffraction peaks were observed with all the samples, irrespective of the calcination temperature, which only affected the intensity of the reflection. They have become less pronounced, but most of all widened, in the nanosheets (exfoliated samples at 120 W power) mainly due to concurrently reduced plane size of the layers following the exfoliation treatment.[55]

Table 3. Textural properties of bulk and exfoliated samples.

Sample	BET Surface Area (m^2/g)	Total Pore Volume (cm^3/g)	BJH Adsorption Pore Width (nm)
GC550	9.0	0.032	47.1
GC600	6.1	0.027	32.2
GC550-120W	27.7	0.166	29.3
GC600-120W	19.8	0.083	15.7

As photocatalytic activity is mainly dependent on absorption spectrum (range of wavelength it can absorb), bandgap energy (ability to generate electron-hole pairs upon light absorption with energy higher than bandgap), photoluminescence (efficiency of charge separation and transfer in photocatalytic reactions), and surface area, these properties were measured for both bulk and exfoliated materials. Indeed, when a sample undergoes US treatment, the high-power ultrasonic waves can cause changes in the density, pressure, and temperature distribution within the material, which affect both textural and optical properties.

To determine the surface area available for reactants adsorption, N_2 adsorption–desorption technique was applied to assess the textural properties. All the samples returned a type IV isotherm, which corresponds to mesoporous materials. Adsorption and desorption isotherms of all the materials are reported in Supporting Information. Brunauer–Emmett–Teller (BET) elaboration for specific surface area resulted in ca. 15 m^2/g for the as-synthesized g-C_3N_4 and ca. double values for the exfoliated samples at the highest US power tested. The BET surface area and BJH pore size have been detailed in Table 3. The as-prepared samples treated at 550 °C had 50% higher surface area than the one prepared at 600 °C. Thermal annealing at higher temperature provoked more extensive polymerization and condensation processes, leading to a more compact and less porous structure.[56] This reduces the overall surface area. Furthermore, prolonged exposure to high temperatures can lead to partial thermal decomposition of the material, which can further reduce the surface area.[57]

US input power showed a direct correlation with the surface area of the materials. Increasing the probe ultrasound power led to an increase of specific surface area, indicating more accessible

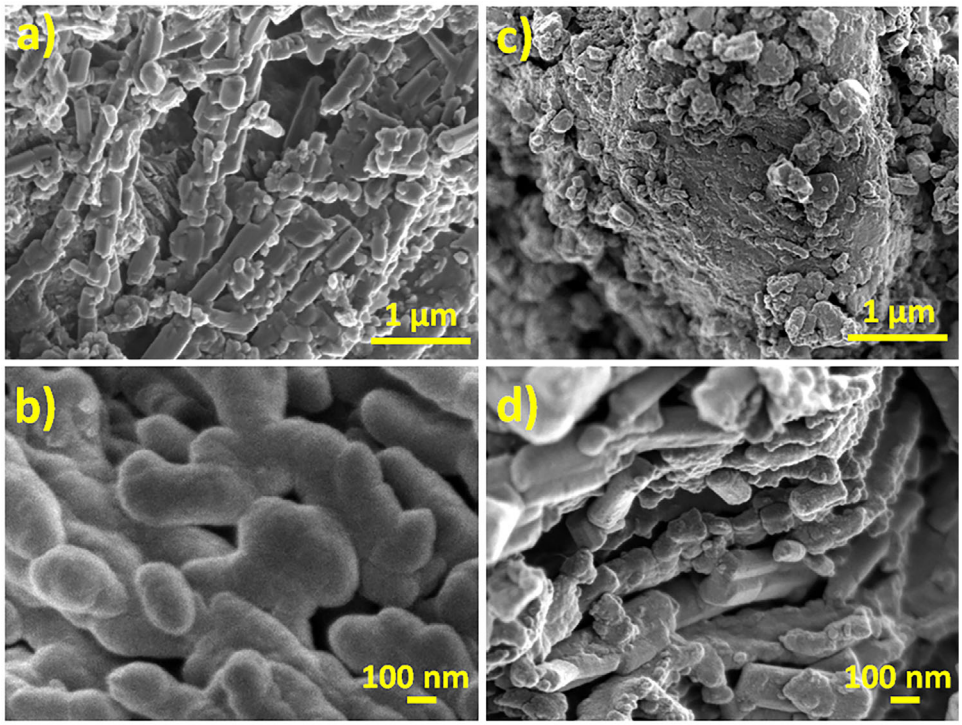

Figure 2. FE-SEM images of exfoliated g-C_3N_4: a) and b) GC550-120 W and c) and d) GC600-120 W.

layers structure with reduced thickness with respect to the bulk precursor. Furthermore, separation efficiency of photogenerated electrons and holes can be improved upon exfoliation, limiting recombination phenomena between stacked layers and favoring the interaction of charge carriers with more abundant adsorbed reactants rather than with recombination sites.

The sample GC550-120 W had higher surface area and pore size with respect to GC600-120 W, which correlates well with the XRD pattern (broader and less intense reflections for the sample calcined at lower temperature, i.e., smaller crystallites). The higher surface and porosity provide more active site for adsorption of the reactant; as a result, higher performance is expected. It should be highlighted here that usually high surface area is not considered of paramount importance for photocatalytic applications If this may be strictly true, it is out of doubt that increasing the availability of adsorption sites for the reactants allows improved probability of productive events with the photogenerated charges rather than dissipative recombination ones.

The FE-SEM images depict a morphology with an overlap of multiple nanosheets (Figure 2a,b), which demonstrate exfoliation of the material into thin pseudo-lamellar form. The 3D analysis of the surface has been elaborated by using the Image J software (Figure 3). The sample GC550-120 W showed a slit-shaped surface, with 30 nm deep valleys, whereas the sample GC600-120 W evidenced a rougher surface with ca. 30% lower valley depth (ca. 20 nm). We observed a few layers thin sheet-like morphology in Figures 2 and 3.[58]

Transmission electron microscopic analyses were performed on the GC550 and GC550-120 W samples. The TEM images show accordance with the FE-SEM images, depicting an overlap of multiple nanosheet and the formation of curled thinner pseudo-lamellar structures in the GC5520-120 W compared to the GC550 (Figures 4, S1, and S2).

Among the numerous diffraction pattern registered on the GC550-120 W, many of them presented an elongated diffraction ring pattern (Figures 4(3b) and S3). This kind of diffraction pattern is typical of overlapping leaflets but with preferential orientations. Exfoliation affects the deformation of nanosheets, leading them to a preferential orientation. From a qualitative point of view, the bulk GC550 showed higher crystallinity compared to the exfoliated GC550-120 W, and this is confirmed by XRD analysis. It is worth pointing out that the thin sheet of the sample showed a tendency to transform into amorphous material under the electron beam (accelerated at 200 kV).

The d spacings have been measured both for GC-550 and GC-550–120 W, reported in Figure 4(2a) and (2b), respectively. The nonexfoliated sample (GC-550) shows a d spacing of ~0.70 nm, whereas the exfoliated sample (GC-550–120 W) has a measured d spacing of ~0.36 nm. These results are confirmed by XRD analysis. The 0.70 nm d spacing is associated with in-plane d spacing and corresponds to the (100) plane, as seen from the XRD reflection at 13°. The 0.35 nm d spacing observed in Figure 4(2b) is due to (002) plane, which reflects the interlayer stacking of conjugated aromatic segments, responsible for the peak at ~27.7°. The values obtained are compatible with those reported in literature for mesoporous g-C_3N_4,[59] which are ~0.68 and ~0.32 nm, respectively, although the measured interlayer d spacing shows slightly higher values. In any case, the effect of exfoliation is evident in the decrease of the extension of the ordered stacked layers. More TEM images and diffraction pattern of both the bulk

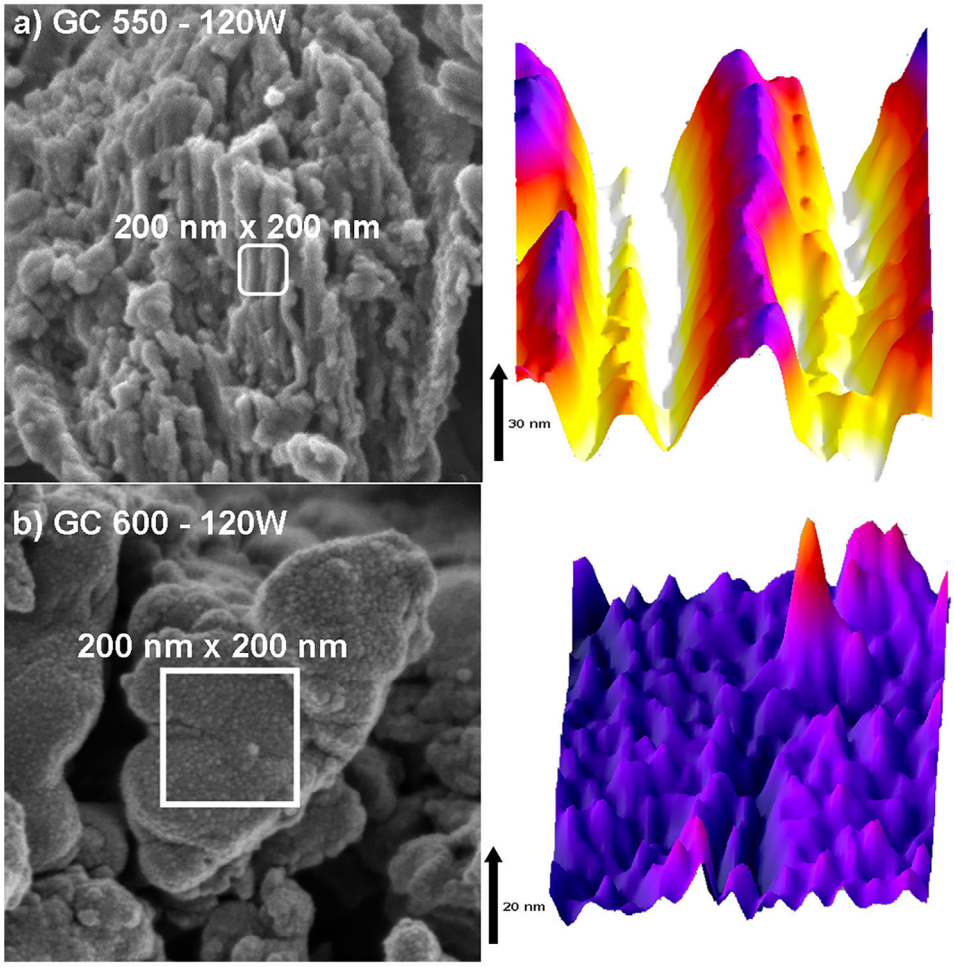

Figure 3. 3D analysis of a) GC550-120 W and b) GC600-120 W.

C_3N_4 and the exfoliated GC550-120 W are reported in Supporting Information (Figures S1–S3).

While performing EDS analysis on the exfoliated sample GC550-120 W, the measured nitrogen content showed a decrease with time, highlighting a strong compositional instability of the exfoliated sample under the electronic beam.

To confirm the theoretical composition elemental analysis was then performed on both GC550 and GC550-120 W samples. CHN tests returned the values expected, showing a slight decrease, if any, in nitrogen content in the case of GC550-120 W compared to GC550 (59.6% versus 60.3% w/w) and a small increase in carbon, hydrogen, and oxygen in the exfoliated sample, possibly due to surface interaction with water. The results of the elemental analysis have been detailed in Table 4.

Optical properties such as bandgap and photoluminescence were investigated by diffuse reflectance spectroscopy and photoluminescence experiments (Table 5; Figures 5 and S4–S11).

The bandgap energy (energy gap between the nearest occupied and unoccupied energy levels) of a photocatalyst is related to its ability to generate electron-hole pairs upon absorption of a radiation with appropriate wavelength. Thus, the bandgap energy (E_g) was measured by DRS and by adopting the Tauc plot method for data elaboration (see Figures S4–S10 and details for elaboration in Supporting Information).[51]

The absorption edge of thin sheet (exfoliated few layers)[51] materials displays a notable blueshift from 473 to 425 nm (Figure 5), which corresponds to increased bandgap from 2.65 to 2.78 with respect to the bulk GC550 (Table 5).[38] This larger bandgap is compatible with the quantum confinement effect of 2D monolayers[38] that are produced as a result of the increase in exfoliation power.

It is worth noticing that all samples have a bandgap and band energy levels that are sufficiently large to overcome the endergonic character for the CO_2 reduction.

The photophysical properties have been investigated for both GC550 and GC600 samples and their US-exfoliated derivatives. A summary of the results is reported in Figures 5 and S11–S18 and Tables 5 and S1.

An important parameter used in estimating the efficiency of photocatalytic activity is photoluminescence quantum yield (Φ). Generally, the stronger the photoluminescence quantum yield, the superior the ability of recombination of the photoexcited electron-hole pairs and thus the lower the photocatalytic activity of the photocatalyst. As presented in Figures 5b and S11b, all the samples display a Φ that depends on the

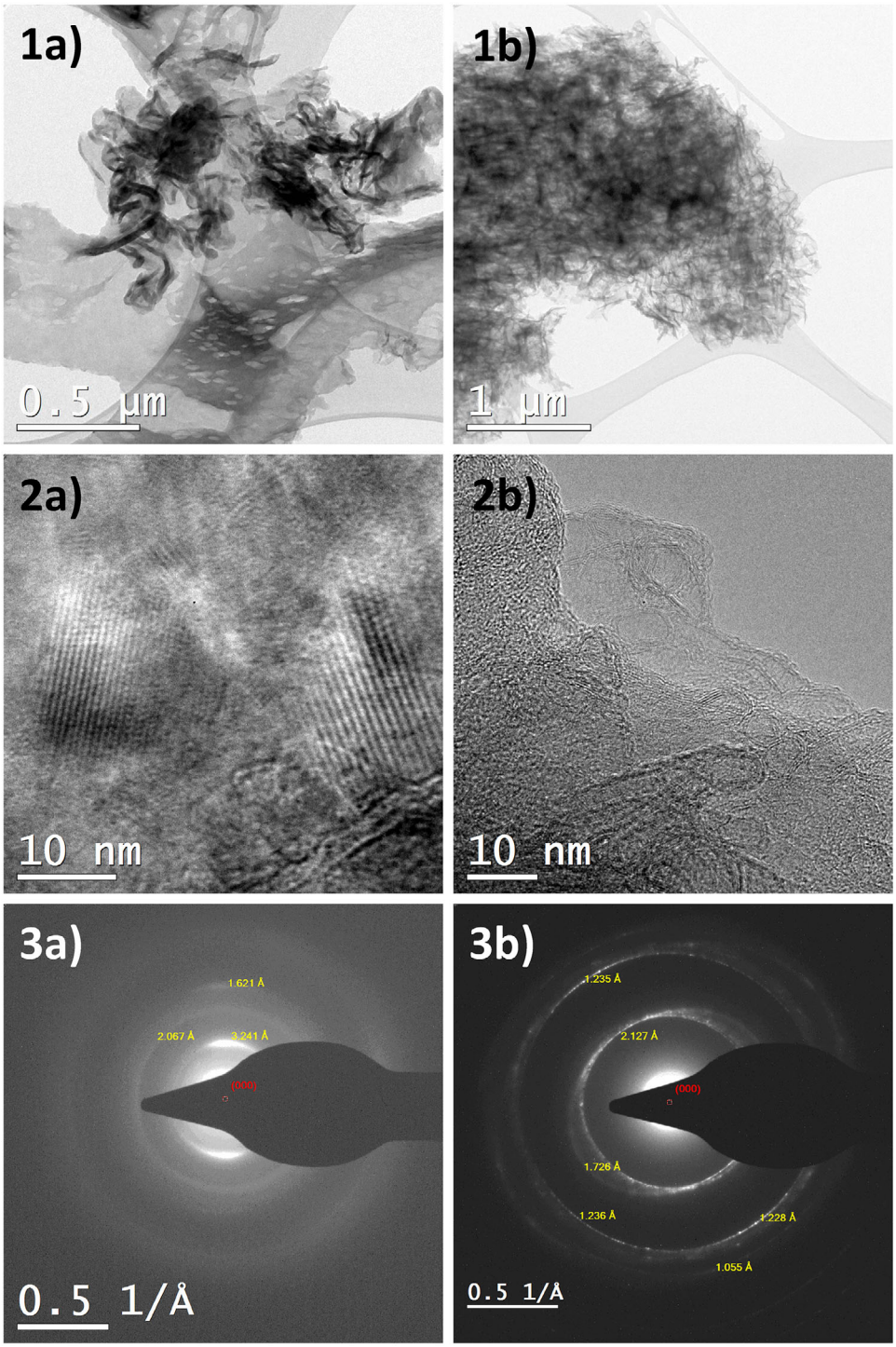

Figure 4. TEM images and diffraction patterns of a) GC550 and b) GC550-120 W.

Table 4. Elemental analysis of bulk and exfoliated samples.

Sample	C (Carbon) (%)	H (Hydrogen) (%)	N (Nitrogen) (%)	O (Oxygen) (%)[a)]
GC550	34.80	1.90	60.32	2.98
GC550-120W	34.90	2.03	59.56	3.51

[a)] O has been calculated as difference.

Table 5. Optical and photophysical properties of the as-synthesized graphitic carbon nitride and US-exfoliated samples at different US power.

	Sample	Bandgap (eV)	λ_{max} [a] (nm)	Φ (%) E_x 290 nm	Φ (%) E_x 360 nm	τ λ_{ex} = 374 nm→ λ_{em} = λ_{max}
1	GC550	2.65	466	4.4	6.6	τ_1 = 8.11 ns (55.69%) τ_2 = 49.91 ns (44.31%)
2	GC600	2.66	463	4.1	5.3	τ_1 = 7.94 ns (53.12%) τ_2 = 63.86 ns (46.88%)
3	GC550-30W	2.73	461	6.3	7.9	τ_1 = 4.77 ns (50.09%) τ_2 = 19.73 ns (31.40%) τ_3 = 142.06 ns (18.51%)
4	GC550-60W	2.76	460	5.7	7.3	τ_1 = 5.19 ns (44.28%) τ_2 = 23.24 ns (34.44%) τ_3 = 148.10 ns (21.28%)
5	GC550-90W	2.77	447	5.3	7.2	τ_1 = 4.60 ns (41.38%) τ_2 = 18.05 ns (38.65%) τ_3 = 153.66 ns (19.97%)
6	GC550-120W	2.78	439	4.7	6.7	τ_1 = 5.07 ns (46.76%) τ_2 = 20.34 ns (33.28%) τ_3 = 158.48 ns (19.96%)
7	GC600-120W	2.69	444	3.1	3.9	τ_1 = 5.06 ns (45.49%) τ_2 = 21.49 ns (35.53%) τ_3 = 156.97 ns (18.98%)

E_x, excitation wavelength; Φ, quantum yield; τ, lifetimes.
[a] Wavelength of the maximum peak of the emission spectrum exciting at 360 nm.

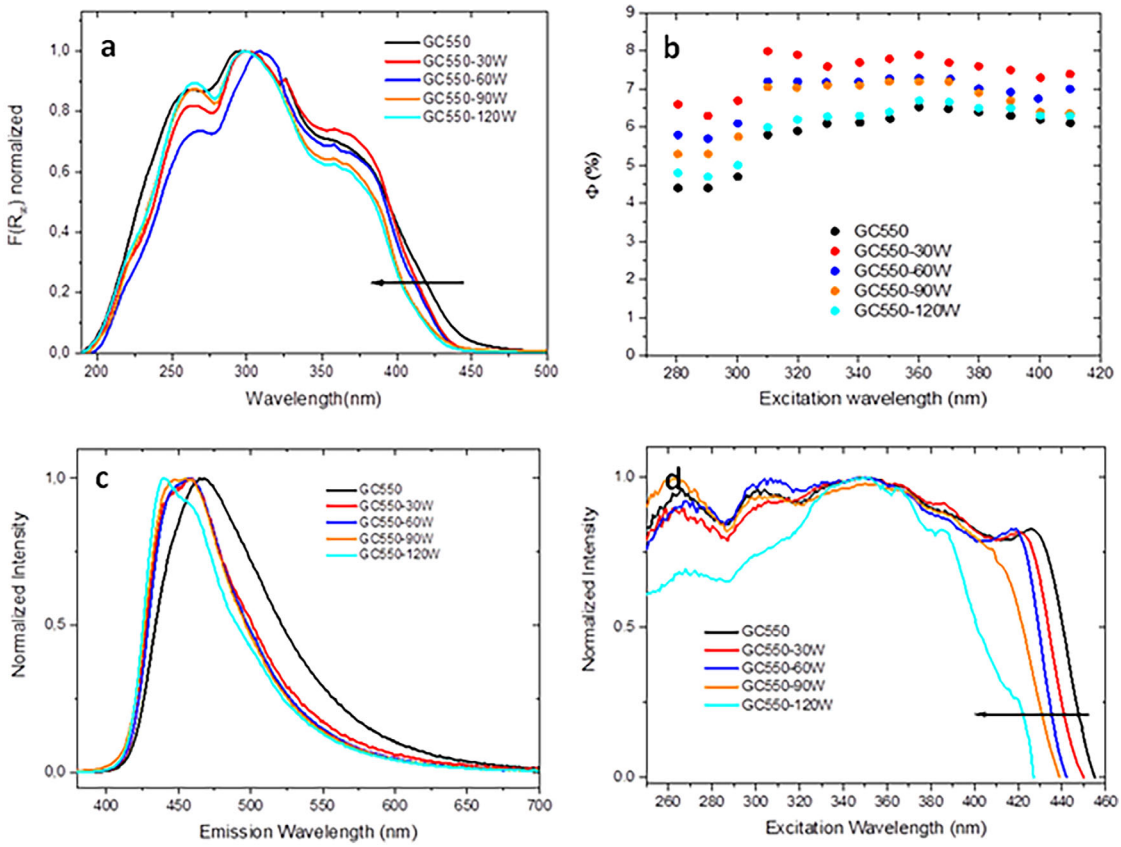

Figure 5. Results obtained from g-C_3N_4 calcined at 550 °C: a) normalized Kubelka–Munk function, b) photoluminescence quantum yield (Φ), c) normalized emission spectra (excitation wavelength at 360 nm), and d) normalized excitation spectra of the as-synthesized g-C_3N_4 and exfoliated samples. Arrow marks in (a) and (d) represent a systematic blueshift with increasing exfoliation power.

excitation wavelength; in particular, from 280 to 300 nm, the Φ was always lower than in the 310–410 nm, indicating increased radiative transitions in the lowest energy excitation region. Moreover, the as-synthesized GC550 sample exposed Φ lower than the exfoliated samples for all excitation wavelengths, whereas the sample exfoliated at 30 W returned the highest value, followed by 60, 90, and 120 W (in Table 5, the Φ value is shown for two representative excitations at 290 and 360 nm). Interestingly, both the as-synthesized g-C_3N_4 and the exfoliated sample at 120 W have comparable Φ values. Normalized emission spectra of the as-synthesized g-C_3N_4 and exfoliated samples are shown in Figures 5c and S11c. The emission spectrum of the as-synthesized g-C_3N_4 has a maximum peak around 466 nm, which is in line with results for powders obtained by thermal condensation process of melamine at 550 °C.[60] In contrast, exfoliated samples were slightly blueshifted to 461, 460, 447, and 439 nm with increasing exfoliation power to 30, 60, 90, and 120 W, respectively. A blueshift was further observed in case of normalized excitation spectra monitored at the emission peak wavelength of each sample (Figures 5d and S11d). The excitation spectrum of the as-synthesized g-C_3N_4 calcined at 550 °C exhibited a broad band covering from 250 to 455 nm, which was slightly shifted at higher energy as the exfoliation power was increased. The observed blueshifts in the excitation and emission spectra of the exfoliated samples are a further confirmation of the bandgap expansion due to the quantum confinement effect following the exfoliation process, as already noted in the absorption spectra (Figures 5a and S11a). It is believed that high input power ultrasound is likely to facilitate lifetime of photogenerated electrons by creating nanostructures within the material for the photogenerated electrons to traverse, which can increase their lifetime by delaying recombination with holes.

Time-resolved fluorescence decay measurements of the samples are displayed in Figures S12–S18 with the relative fit. For the as-synthesized GC550, a biexponential decay was used with two lifetimes of 8.11 and 49.91 ns. On the contrary, for the exfoliated samples a triexponential decay was necessary to provide the best match between the measured data and the calculated decay. Table 5 details the lifetime values for the samples calcined at 550 and 600 °C, as-synthesized and subsequently US-exfoliated. The first two lifetimes were of the same order of magnitude with respect to those obtained for the as-synthesized g-C_3N_4, whereas the third lifetime was significantly longer. This latter value was absent in the nonexfoliated material, whereas it increased progressively to 142.06, 148.10, 153.66, and 158.48 ns as the exfoliation power was increased stepwise from 30 to 120 W. Similar lifetimes were observed for the as-prepared GC550 and GC600 samples and, accordingly, also for the counterparts exfoliated at 120 W power. Only slightly lower lifetime was observed for τ_3 in the exfoliated samples calcined at the highest temperature.

Such behavior was consistent with the presence of two emissive species involved during the fluorescence decay. Specifically, the two shorter lifetimes can be correlated to the recombination of the photogenerated electron-hole pairs in the bulk g-C_3N_4 structure, whereas the third lifetime to the recombination of the photogenerated electron-hole pairs along the plane of the exfoliated 2D monolayers.[61,62] As the US power is increased, the exfoliation process becomes more efficient, producing increasingly thinner layers (exfoliated few layers). Consequently, the third lifetime increases, approaching the theoretically predicted value of 260 ns for an exciton radiative lifetime of a single 2D monolayer.[47] By suppressing electron-hole recombination, longer exciton lifetimes can be produced, thus, increasing the chances of exciton usage in photocatalytic reactivity.

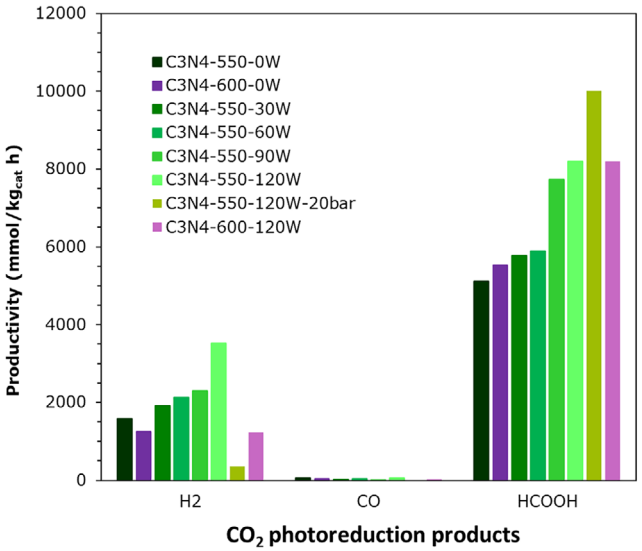

Figure 6. CO_2 photoreduction on g-C_3N_4 catalysts, T = 80 °C, P = 8 bar, HS = 1.66 g/L, catalyst loading = 0.031 g/L, reaction time 24 h. Comparative test with sample GC550-120 W at 20 bar.

3.2. Photoreduction of CO_2 Activity Data

Photoreduction of CO_2 may lead to a series of liquid and gaseous products such as CO, H_2, CH_4, HCHO, HCOOH, and CH_3OH. Formation of these products is dependent on catalysts and reaction conditions (e.g., pH, pressure, time, catalyst mass, and hole scavenger). For instance, neutral pH favors methanol formation, whereas basic pH allows formic acid as the major product with very high selectivity and productivity.[46] A scheme with the proposed mechanism is reported in Scheme S1, based on an extensive description reported elsewhere.[63] Briefly, when operating at basic pH, the only product resulted HCOOH, at least until the full consumption of the hole scavenger, after which the formed HCOOH started to act as scavenger itself producing also H_2 and CO through photoreforming.

Applying the fabricated catalysts in our specially designed reactor, CO_2 photoreduction reaction was performed under light irradiation at 365 nm maximum wavelength, at 80 °C, and 8 bar pressure (Figure 6 and Table 6). Table 6 lists the performance of all the materials, which produced formic acid as a major product with some smaller portions of CO and H_2.

Blank reaction was carried out either without irradiation or without photocatalyst or without sodium sulfite as hole scavenger. The results demonstrated in every case a negligible productivity for any product.

Table 6. Summary of the hole scavenger conversion and productivity to various products catalyzed by as synthesized and exfoliated samples. Testing conditions $T = 80$ °C, $P = 8$ or 20 bar, HS = 1.66 g/L and catalyst loading = 0.031 g/L, reaction time 24 h.

Entry	Sample	Formic Acid (mmol/kg_{cat} h)	Carbon Monoxide (mmol/kg_{cat} h)	Hydrogen (mmol/kg_{cat} h)	HS Conv. (After 24 h)
1	GC550	5121	43	1587	90.34
2	GC600	5527	52	1254	89.21
3	GC550-30 W	5722	20	1917	90.93
4	GC550-60 W	5898	41	2132	90.31
5	GC550-90 W	7732	12	2292	89.98
6	GC550-120 W	7930	62	3513	93.12
7	GC600-120 W	8203	28	1243	90.41
8	GC550-120 W 20 bar	10,005	16	365	94

The as-synthesized materials prepared at 550 and 600 °C returned 5121 and 5527 mmol/kg_{cat}/h FA, respectively. A further improvement to 5722 and 5898 mmol/kg_{cat}/h was noticed in reactions catalyzed with exfoliated sample at 30 W and 60 W power US, respectively. Among all exfoliated catalysts tested, GC600-120 W showed highest productivity of FA (8203 mmol/kg_{cat}/h), which is slightly higher but still comparable to the result achieved with catalyst GC550-120 W (7930 mmol/kg_{cat}/h) (Table 6).

The increasing trends of formic acid productivity with increasing input power correlates well with the BET surface area increase reported in Table 3 and in general with the XRD evidence of progressively higher exfoliation with increasing US power.

By increasing pressure from 8 to 20 bar, the productivity of formic acid boosted up further to 10,005 mmol/kg_{cat}/h for sample GC550-120 W, that is, ca. 20%–25% productivity increase (Figure 6 and Table 6).

Lower productivity of gaseous products with increasing pressure is also observed, in line with improvement in FA productivity (Table 6), which is in agreement with the Le Chatelier principle and previous results at variable pressure.[46] The gas phase products were mainly H_2 and some CO (plus excess CO_2, not quantified) and syngas formation was attributed to the subsequent photoreforming of the organic products formed by photoreduction of CO_2 once the hole scavenger (HS) was consumed. Indeed, the reaction was carried out in presence of sodium sulfite as HS and H_2 was indeed becoming visible only after the consumption of most of the inorganic HS, added at the beginning of the reaction (>80% HS conversion).[47,64]

The hole scavenger plays a crucial role: when absent, a negligible productivity is achieved, and among different compounds, a substantially higher reactivity than for organic compounds (alcohols, amines) has been achieved with Na_2SO_3.[46,64] The increase of hole-scavenger concentration also resulted in higher formic acid productivity (at basic pH) at the expenses of gaseous products. The results showed that doubling the hole-scavenger concentration led to four times higher formic acid productivity with ca. halved hydrogen productivity.

After 24 h-long activity test, practically full conversion of the HS was observed for every sample and GC550 showed higher productivity toward H_2 and CO with respect to sample GC600. Correspondingly, the FA productivity of GC600 was slightly higher than that of the GC550 catalyst. As said, FA is the starting reagent for the chain reaction of CO_2 photoreduction and consecutive photoreforming of FA to form syngas; thus, it may be concluded that the sample GC550 was overall more active than GC600 as it not only accumulated until consumption of the HS, but also significantly favored the consecutive photoreforming reaction. Accordingly, sample GC550-120 W produced higher amount of CO and H_2 than GC600-120 W when tested for 24 h reaction time (Table 6), which testifies an overall higher activity of the GC550 sample. Indeed, the sample GC550-120 W had higher surface area with respect to GC600-120 W, which can provide higher number of active sites for the reactants (Table 3).

As evidenced in Table 5, GC550-120 W provided a low quantum yield (i.e., low efficiency of dissipative charge recombination events) and the longest τ_3, which is attributed to longer lifetime for photogenerated charges against dissipative recombination.

In order to better compare the efficiency of the photoreduction reaction when different products are obtained and to have a quantitative assessment of the utilization of the input radiation, we have calculated the energy stored in the products (from the productivity and the higher or lower heating value, HHV or LHV, of each compound) with respect i) to the energy consumed by the lamp during the irradiation time or ii) to the effective irradiance hitting the sample during the test. Tables 7 and 8 summarize the calculated efficiency of fabricated samples.

According to the data, the samples GC600-120 W and GC550-120 W achieved 0.020% and 0.024% efficiency, respectively, when calculated based on lamp consumption (Case i). Thus, we can confirm that the sample GC550-120 W has higher activity compared to the sample calcined at 600 °C and exfoliated at the same US power.

Exfoliated 2D graphene-like structures provide higher surface area with respect to the bulk g-C_3N_4. Plus, the generated charge carriers (electron-hole) can reach faster the surface for performing a reduction reaction due to the shorter length compared with the bulk structures. Applying ultrasound waves to the solution results in the generation of nanometric-bubbles, which when collapsed, produce higher amounts of energy and pressure. The collapsed bubbles can overcome the van der Waals

Table 7. Efficiency of photoreduction process of fabricated samples based on energy stored in the major products calculated based on higher heating value (HHV).

Energy Stored Based on HHV					
Sample	H_2	HCOOH	Total	Efficiency (%)[a]	Efficiency (%)[b]
GC550	318	1250	1568	0.014	0.180
GC600	403	1158	1561	0.014	0.179
GC550-30 W	487	1305	1792	0.016	0.206
GC550-60W	541	1333	1875	0.017	0.216
GC550-90W	582	1748	2330	0.021	0.268
GC550-120W	893	1793	2686	0.025	0.309
GC600-120W	316	1855	2170	0.020	0.250
GC550-120 W 20 bar	219	2262	2481	0.023	0.285

[a] Efficiency calculated based on energy consumed by the UV lamp.
[b] Efficiency based on measured irradiance and average irradiated surface in the reactor.

Table 8. The efficiency of photoreduction process of fabricated samples based on energy stored in the major products calculated based on Lower Heating Value (LHV).

Energy Stored Based on LHV					
Sample	H_2 (kJ/mol)	CHOOH (kJ/mol)	Total	Efficiency (%)[a]	Efficiency (%)[b]
GC550	269	1030	1299	0.012	0.149
GC600	341	954	1295	0.012	0.149
GC550-30 W	411	1075	1487	0.014	0.171
GC550-60W	458	1099	1556	0.014	0.179
GC550-90 W	492	1440	1932	0.018	0.222
GC550-120 W	755	1477	2232	0.021	0.257
GC600-120 W	267	1528	1795	0.017	0.206
GC550-120 W 20 bar	185	1864	2049	0.019	0.236

[a] Efficiency calculated based on energy consumed by the UV lamp.
[b] Efficiency based on measured irradiance and average irradiated surface in the reactor.

forces between layers of g-C_3N_4. Moreover, the power of ultrasound has a great impact on the rate of generated bubbles and collapse energy (different nanometric bubbles' sizes). Thus, varying the power of a probe-ultrasound can lead to differently exfoliated samples. XRD analysis qualitatively showed the effects of power on the exfoliation efficiency, that is, the sample with lower reflections intensity and wider peak broadening was characterized by looser interplane interaction (more exfoliated).

As the bandgap of GC550-120 W, as measured by DRS, was slightly higher than for other samples, we can conclude that a reasonably small blueshift of the absorption edge of the sample does not penalize much the activity, provided that the irradiation is performed with higher energy than the bandgap.

Much more significantly, the reason of higher activity is, on one hand, correlated to the low quantum efficiency, similar for GC550-120 W to the nonexfoliated GC550 material. This means lower efficiency in emissive relaxation and thus higher availability of the photogenerated charges for the proposed surface reactions. However, in addition, all the exfoliated samples showed a third characteristic time in fluorescence spectra, which was attributed to the increased lifetime of the photogenerated charges due to limited recombination through the stacking layers. Such time was significant only for exfoliated materials and increased progressively with the US-exfoliation power, indicating progressively longer lifetime with increasing exfoliation. This explains the higher activity of GC550-120 W with respect to the nonexfoliated bulk equivalent.

Besides the reaction at 8 bar, the most reactive sample was tested at higher-pressure (20 bar) to further boost the formic acid productivity. As expected, ca. 10 mol FA/kg_{cat} h (Table 6 and Figure 6), corresponding to 0.46 kg FA/kg_{cat} h, was obtained, which is one of the highest productivities reported until now. The efficiency resulted comparable to that achieved with the same sample at 8 bar due to different products distribution. Indeed, higher pressure disfavors photoreforming and products evolution in the gas phase, so it is possible to tune both efficiency and products selectivity by playing with conditions (pressure and pH), besides catalyst formulation.

It may be questioned if the C comes really from CO_2 or maybe from the catalyst. The answer comes from the comparison of the amount of C in the product obtained and in the catalyst used. Imagining all the C contained in the catalyst put

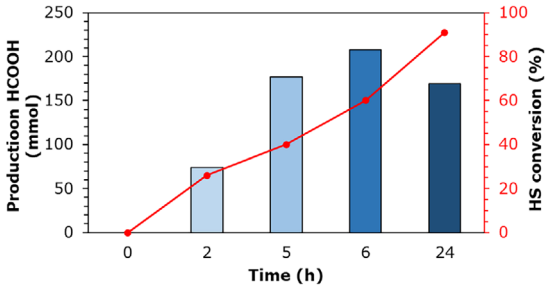

Figure 7. Kinetic test of CO_2 photoreduction on GC550-120 W. Absolute productivity reported for FA.

in the photoreactor should convert to HCOOH, and this is not supported by the evidence that solid catalyst remains suspended in water after the test and its activity remains unaltered with recycling, this would correspond to ca. 1.2 mmol of HCOOH. This value should be compared with ca. 9 mmol HCOOH formed in a conventional test. The reactor does not contain other carbon sources, so the contribution of CO_2 reduction is demonstrated.

3.3. Effect of Reaction Time on Hole Scavenger Consumption and Products Distribution

Tests were also performed to study CO_2 photoreduction on the best performing exfoliated g-C_3N_4 (GC550-120 W) at variable reaction time. Every 2 h, 20 mL of the solution was withdrawn and analyzed. Withdrawing the gaseous samples led to a decrease of pressure, and for this reason, the reactor was pressurized again to 8 bar after each sampling. The performed test confirmed that formic acid was the dominant product till hole-scavenger conversion was almost complete. As shown in Figure 7, the formic acid production significantly increased until >70% of the hole-scavenger was consumed. Then, after ~ca. 6 h, the concentration of formic acid started decreasing as the formic acid worked as a hole-scavenger itself when the concentration of Na_2SO_3 was no more sufficient to close the circuit of the photogenerated charges consumption. Products such as carbon dioxide, carbon monoxide, and hydrogen were produced consequently. Their absolute value should be considered only qualitatively for this specific test due to some dilution upon pressurization with CO_2, which was needed, as said, after each sampling. Nevertheless, despite this progressive dilution their increase of concentration was significant.

It is also worthy to note that during the first 6 h of the reaction, no gaseous products were detected, which is in line with the findings of our previous studies.

3.4. Role of Input Energy (Power) in Exfoliation for Properties Enhancement

US input power can bring changes in structure, morphology (nanoparticles or agglomerates), crystallinity, and chemistry of g-C_3N_4. The mechanical stress and cavitation due to high US power can result in formation of cracks and defects on the surface of g-C_3N_4. The defects may act as an additional active site for the reaction or possibly as recombination centers. Weak van der Waals interaction within layers allows exfoliation of carbon nitride to reduce thickness and increase surface area for enhanced surface adsorption, light exposure, and charge separation/transportation.[32,33] Similarly, the interlayer pattern of the melon units, joined through H bonds, can be cleaved selectively to induce desirable properties such as absorption of wide range of light for improved photocatalytic activity. Moreover, g-C_3N_4 can be easily prepared by thermal polymerization of carbon- and nitrogen-rich precursors (such as urea, melamine, cyanuric acid, thiocyanuric acid, cyanuric chloride, dicyanamide, urea, and triazinetrihydrazine).

The polymeric structure can further allow modification during synthesis or post-treatment processes without damaging the g-C_3N_4 framework. Eventually, attempts with thermal,[65] mechanical,[66] chemical,[38,67,68] mechanochemical,[69] and ultrasound[41] induced exfoliation of g-C_3N_4 have been proposed. This resulted in improved catalytic efficiency by promoting charge transfer, mobility, and separation through significant increase in accessible surface area. Among the possible treatments, exfoliation by liquid phase–assisted ultrasound is particularly attractive as it does not cause structure or composition changes along with fast, easy, and comparatively less hazardous features. The activity of our water-mediated exfoliated materials (GC550-120 W and GC600-120 W) displayed among the highest in the literature with ~8.2 mol/kg_{cat}/h for formic acid production. This value further increased to ca ~10 mol/kg_{cat}/h when increasing pressure to 20 bar.

Cai et al. studied sonication time and input power to exfoliate graphite into graphene nanoplates and found that higher input power and extended time led to high optical density.[70] It is likely that GC550-120 W and GC600-120 W (materials exfoliated at high input power) obey to the same feature that could facilitate their light harvesting properties. Similar observation to thin layer materials was also achieved tuning different parameters, including input power, frequency, and time.[71,72] More recently, high ultrasonic frequency is reported to lead larger and multilayered 2D materials into fewer layer flakes.[41] Nonetheless, use of expensive and toxic solvents with high boiling points are critical challenges, which stresses careful handling and storage. Possible agglomeration during slow evaporation of solvents is another issue during flake deposition onto the substrate. Moreover, majority of literature suggests use of strong acids, polymer, or surfactants as stabilizers to enhance exfoliation process of g-C_3N_4, necessitating postprocessing removal of residuals. This may reduce performance or stability of materials. Thus, it is necessary to maintain quality and properties of the particles by investigating exfoliation techniques of low-cost, eco-friendly, and low boiling solvents without additional surfactants or stabilizers. Some of the most relevant reports concerning CO_2 photoreduction to formic acid over g-C_3N_4-based catalysts are summarized and reported in Table 9.

Despite several attempts to advance the field, the effect and role of input power in sonication are poorly understood and scarcely discussed in the literature, resulting in low exfoliation efficiency. The power of the sonication determines the intensity

Table 9. Comparison of literature studies on photoreduction of CO_2 using g-C_3N_4-based catalysts.

Entry	Catalyst	Catalyst Preparation Method	Catalytic Test Operating Conditions	Main Product(s)	Reference
1	Bulk g-C_3N_4 (2.77 eV bandgap)	Thermal condensation of dicyanadimide (550 °C for 4 h in static air)	20 mg catalyst, 0.06Mpa, pressure, 300 W Xe lamp; UV and visible range (>400 nm)	CH_3CHO (~0.4 μ mol in 5 h under UV, and ~0.24 μ mol in 5 h under visible light	[78]
2	g-C_3N_4 nanosheets (2.97 eV bandgap)	Thermal oxidation etching of bulk g-C_3N_4 (550 °C for 2 h)	20 mg catalyst, 0.06Mpa, pressure, 300 W Xe lamp; UV and visible range (>400 nm)	CH_4 (~0.1 and ~0.024 μmol h^{-1} under UV and visible light, respectively)	[78]
3	Porous g-C_3N_4 (2.83 eV bandgap)	Thermal polymerization of melamine hydrochloride at 500 °C for 2 h with a heating rate of 20 °C min 1, followed by a further heat treatment at 520 °C for 2 h	CO_2: 1 atm, catalyst:100 mg, glass reactor with area of 4.2 cm^2, light 300 W Xe lamp, volume of reaction mixture: 230 mL, DI water: 0.4 mL, visible light (>420 nm)	CO (0.41 mM h^{-1})	[79]
4	Bulk g-C_3N_4 (2.70 eV bandgap)	Thermal polymerization of melamine at 500 °C for 2 h with a heating rate of 20 °C min 1, followed by a further heat treatment at 520 °C for 2 h	CO_2: 1 atm, catalyst:100 mg, glass reactor with area of 4.2 cm^2, light 300 W Xe lamp, volume of reaction mixture: 230 mL, DI water: 0.4 mL, visible light (> 420 nm)	CO (0.41 mM h^{-1}) CO (1.9 mM h^{-1})	[79]
5	Red phosphor/g-C_3N_4 hybrids	Thermal polymerization of urea at 550 °C for 4 h in Ar atmosphere, followed by annealing with red phosphor	0.5 wt% Pt loaded PCN-x hybrids (20 mg); 500-W xenon arc lamp, 0.2 ml ultrapure water	295 μmol $h^{-1}g^{-1}$	[80]
6	Ru/mpg-C_3N_4		Ru on mpg-C_3N_4 (8.0 mg); mixture of acetonitrile–triethanolamine (4:1v/v) 4 mL; reaction vessel, Pyrex test tube light: 450 W Xe lamp with a $NaNO_2$ solution filter	Formic acid 19.345 μmol/5 h	[81]
7	Indirect Z-scheme BiOI/g-C_3N_4	BiOI/g-C_3N_4 is synthesized by deposition method using $Bi(NO_3)_3{\cdot}5H_2O$ and g-C_3N_4 and glycol	CO_2/H_2O, stainless steel cylindrical vessel, light: 300 W Xe arc lamp with a UV cutoff filter (λ > 400 nm), catalyst: 100 mg dispersed on glass dish equipped with a quartz window for passing irradiation	CO (17.23 μmol)	[82]
8	Pt-loaded g-C_3N_4	Bulk g-C_3N_4 was prepared by the thermal polycondensation of urea. Pt/CN photocatalyst was synthesized via a polyol process by ultrasonicating bulk g-C_3N_4 in ethylene glycol followed by slow addition of $H_2PtCl_6{\cdot}6H_2O$	CO_2: 5 mL/min, ambient temperature and pressure, visible light source: 15 W energy saving day light bulb	CH_4 (13.02 μmol g_{cat}^{-1})	[83]
9	2% Pt/g-C_3N_4	Thermolysis of thiourea at 550 °C and postimpregnation for Pt incorporation. Ultrasonication for 1 h	Pyrex reactor at ambient temperature and atmospheric pressure. 100 mg of the sample was put into the glass reactor and 10 mL of deionized water was added. CO_2 and H_2O vapor were in situ generated by the reaction of $NaHCO_3$ (0.12 g, introduced into the reactor before seal) and HCl aqueous solution (0.25 mL, 4 M) which was introduced into the reactor using a syringe	CH_4 (~0.12 μmol) and CH_3OH (~ 0.10 μmol)	[84]

Table 9. (Continued)

Entry	Catalyst	Catalyst Preparation Method	Catalytic Test Operating Conditions	Main Product(s)	Reference
10	g-C_3N_4/ZnO	Calcination method utilizing urea and zinc nitrate hexahydrate	300 W Xe Arc lamp.	CH_3OH 0.6 μmol h^{-1} $g_{cat}{}^{-1}$	[85]
11	Z-scheme SnO_2-x/g-C_3N_4 composite	Calcination method utilizing melamine at 520 °C for 4 h	Stainless steel reactor with a quartz window, catalyst: 20 mg, water: 4 mL, CO_2: 0.3 MPa, temp: 80 °C for 4 h, 500 W Xe lamp	CO (~18 μmol $h^{-1}g_{cat}{}^{-1}$)	[86]
12	C_3N_4 modified ruthenium(II) complex		G-L/400W high-pressure Hg lamp λ > 400 nm/MeCN/TEOA	HCOOH (TON 175)	[87]
13	RuP/C_3N_4		Ru-complex (7.8 mmol per gram of C3N4)/C3N4 (8.0 mg) in a mixture of DMA and TEOA (4:1, v/v; 4 mL). A Pyrex test tube with a septum (11 mL capacity) was used as the reaction vessel and a 400 W high-pressure Hg lamp with a $NaNO_2$ solution filter as the light source	HCOOH (TON ~ 1100) and AQY (5.7% at 400 nm) values	[17]
14	g-C_3N_4 / 3% (Cu/TiO_2) composite	Thermal treatment of melamine at 550 °C for 3 h to g-C_3N_4 followed by wet impregnation	CO_2: 20 mL/min; catalyst: 0.1 g and 200 mL of 1.0 M NaOH solution; Double-jacketed Pyrex glass vessel; 500 W, 22 cm long arc Xe-lamp; UV or visible light irradiation, time: 2 h	CH_3OH (2574 mmol $g_{cat}{}^{-1}$) and HCOOH (5069 mmol $g_{cat}{}^{-1}$) under visible light. CH_3OH (614 mmol $g_{cat}{}^{-1}$) and HCOOH (6709 mmol $g_{cat}{}^{-1}$) under UV light irradiation	[88]
15	NS-P g-C_3N_4-Ni	Calcined polymerization of monomeric dicyanadimide and perylendicyanadiamide followed by sonication in IPA to exfoliate into single layer P-g-C_3N_4 nanosheet. Then metallization to NS-P g-C_3N_4-Ni	Under visible-light irradiation (300 W Xe lamp) in 0.5 m $KHCO_3$ aqueous solution without any sacrificial agent	72.3 μmol L^{-1} of formate	[89]
16	NH_2-UiO-66/g-C_3N_4/CdTe		Visible light irradiation (≥400 nm), 300 W Xe lamp	HCOOH (24.6 μmol $g^{-1}h^{-1}$)	[90]
17	g-C_3N_4@CeO_2 (CeO_2 49.7 wt %)	SiO_2 template is synthesized for core-shell g-C_3N_4. Then coupled with CeO_2 gave g-C_3N_4@CeO_2 after NH_4HF_2 washing and heating. Finally, hollow g-C_3N_4@CeO_2 with oxygen vacancies was reduced by H_2 at 500 °C for 6 h. Ultrasound wave for 30 min	300 W Xe lamp (λ > 420 nm)	CH_4 (3.5 μmol g^{-1}), CH_3OH (5.2 μmol g^{-1}), and CO (16.8 μmol g^{-1})	[91]
18	$LaPO_4$/g-C_3N_4	Melamine was dissolved, acidified, and thermally treated at 550 °C to form tubular g-C_3N_4 (tCN) Core-shell nanocomposites were then prepared by sonicating tCN with lanthanum nitrate and $(NH_4)_2HPO_4$ solution	Airtight reactor with optical quartz window, 30 mg of the sample, 80 kPa CO_2 (99.99%) gas, 300 W Xenon-arc lamp	CO (14.43 μmol g^{-1} h^{-1}) on average, which is about 10.36 and 8.07 times as much as those on pure $LaPO_4$ and tCN, respectively	[92]
19	WO_3-x/g-C_3N_4	Hydrothermal and deposition precipitation method. Ultrasonication; 40 kHz for 3 h	500 W Xe lamp (full spectrum)	CO (6.46 μmol g^{-1} h^{-1})	[93]

Table 9. (Continued)

Entry	Catalyst	Catalyst Preparation Method	Catalytic Test Operating Conditions	Main Product(s)	Reference
20	40 wt% g-C_3N_4/$ZnIn_2S_4$	Hydrothermal method, calcination. Thermal exfoliation	300 W Xe lamp (full spectrum)	CO (82.26 μmol g^{-1} h^{-1}), which is 10.1 and 2.8 times as high as those of the g-C_3N_4 and $ZnIn_2S_4$ monomers, respectively	[34]

of the cavitation, which directly affects the extent of the delamination process. High sonication power can reduce the thickness of layered materials through a process called cavitation. During sonication, high-intensity sound waves generate microbubbles in the liquid surrounding the material. When the microbubbles reach a critical size, they rapidly collapse, creating high-energy shock waves that can weaken and disrupt the material's surface. This repeated action of bubble formation and collapse can cause mechanical abrasion, leading to the thinning of the layered material and structural changes. Conventionally, these processes are attributed to the force generated by microjets and microbubbles collapse near the surface of materials. It is believed that g-C_3N_4 exfoliation proceeds via cavitation process, where static pressure of liquid reduces to below the vapor pressure of liquid, forming small cavities. After subjecting to high pressure, these cavities can be turned into the bubbles, a phenomenon which is dependent on solvent environment, container's size, energy input, quantity of raw materials, and even position of the sample in the sonication bath.

As far as US-assisted properties improvements are concerned, the layered materials like carbon nitride may undergo two probable structural modifications during the sonication: (i) exfoliation, where reduction in thickness takes place, and (ii) fragmentation, where reduction in lateral dimension happens. To understand these phenomena, the samples were allowed for sonication in water at different input energy of power, that is, 30, 60, 90, and 120 W while keeping the treatment time constant.

A low input power is expected to achieve limited cavitation and poor exfoliation, whereas on increasing input power to 120 W, the surface area was greatly improved and XRD spectra consistently broadened, as demonstrated in Table 3 and Figure 1. This change happens due to enhancement in cavitation and thus of exfoliation, but it had an additional result of slightly widening the bandgap of as-synthesized g-C_3N_4 from 2.65 to 2.78 eV (Table 5). Similar observation of high input power in increasing surface area and thickness reduction can be noticed in graphene exfoliation.[71]

In addition, there are several other factors that influence the rate of exfoliation and fragmentation. Unlike graphene, a good interaction of solvent with bulk particles of carbon nitride is considered essential for the exfoliation.[73] It is known that stacking of single g-C_3N_4 flakes is mechanically weak, shearing of stacks may happen before fragmentation, and exfoliation to proceed during sonication. Similar phenomenon has been observed in exfoliation for an analogous molecule.[74] Structurally, g-C_3N_4 contains edge plane and base plane active sites.[75] The preference of exfoliation or fragmentation can presumably be also dependent on the ratio between edge plane (E_E) and basal plane (E_S) and the ratio of in-plane and out-of-plane mechanical properties.[76,77]

Therefore, the exfoliation at progressively higher power induces, on one hand, a higher surface area due to increasing minimization of the stacking between adjacent layers and rupture of the layers themselves. More interestingly, these phenomena contribute to a decrease of the recombination rate of the photogenerated charges, visible in lower quantum yield and in the appearance of a third relaxation time during photophysical experiments. On the contrary, this slightly increased the bandgap due to the decrease in size of the primary particles. However, this effect was not affecting the capacity of the material to harvest visible light. Overall, this resulted in significantly increased productivity of HCOOH with increasing exfoliation power.

4. Conclusions

Utilization of CO_2 by photoreduction into formic acid is one of the promising routes to convert this greenhouse gas into a valuable fuel and chemical. Significant productivity has been achieved for this product (up to ca. 10 mol/kg_{cat} h at the pressure of 20 bar and ca. 8.2 mol/kg_{cat} h at 8 bar), which makes it a viable candidate for further optimization and scale up.

g-C_3N_4 revealed a good photocatalyst with tunable physical–chemical properties when obtained by amazingly simple calcination of melamine as inexpensive precursor. Multilayered structures of g-C_3N_4 resulted in poor surface area and relatively limited FA productivity. The approach proposed here allowed to obtain exfoliated g-C_3N_4 by US treatment in water. By controlling the sonication power and parameters, it was possible to optimize the nanostructure formation and to increase the lifetime of photogenerated electrons in the material. Input power of 120 W was found sufficient for obtaining delaminated sheets, resulting in doubled surface area than the bulk material, but a bit wider bandgap (2.78 eV).

The present activity results suggest that increasing the exfoliation US power can directly improve the photocatalytic performance for CO_2 photoreduction due to enhanced surface area and improved lifetime of charge carriers, with limited recombination between detached stacking layers. Nevertheless, the recovered material was separable and recyclable, irrespectively of the US power applied. We hypothesize that US power can

alter catalytic properties of g-C_3N_4 possibly due to modification in structure (due to mechanical stress and cavitation), morphology (nanoparticles), and crystallinity (ordered structure causing enhanced separation of electron-hole pairs). Regardless of extensive interests in the field, the details about enhancement of material properties for photoreduction of CO_2 into high yield of formic acid could be interesting for both academic as well as industrial research for different materials, as exemplified in Table 2.

Acknowledgements

M.I. Alam, I. Rossetti, and G. Ramis gratefully acknowledge the financial contribution of Fondazione Cariplo through the grant 2021–0855, SCORE (Solar Energy for Circular CO_2 Photoconversion and Chemicals Regeneration), funded in the frame of the Circular Economy call 2021. I. Rossetti and G. Ramis acknowledge MUR for funding the project P20227LB45, SCORE2 (Solar-driven COnveRsion of CO_2 with HP-HT photorEactor), within the Piano Nazionale di Ripresa E Resilienza (PNRR) Missione 4 "Istruzione e Ricerca" – Componente C2 Investimento 1.1, "Fondo per il Programma Nazionale di Ricerca e Progetti di Rilevante Interesse Nazionale (PRIN)". I. Rossetti also acknowledges Università degli Studi di Milano for support through the grant PSR 2021 – GSA – Linea 6, "One Health Action Hub: University Task Force for the resilience of territorial ecosystems". This study was carried out within the Agritech National Research Center and received funding from the European Union – NextGenerationEU (Piano Nazionale di Ripresa E Resilienza (PNRR), Missione 4, Componente 2, Investimento 1.4 – D.D. 1032 17/06/2022, CN00000022). This article reflects only the authors' views and opinions; neither the European Union nor the European Commission can be considered responsible for them. I. Rossetti and M. Tommasi also acknowledge specifically the participation and funding of Tasks 8.2.3, 8.3.2, and 8.4.1.

Open access publishing facilitated by Universita degli Studi di Milano, as part of the Wiley - CRUI-CARE agreement.

Conflict of Interests

The authors declare no conflict of interest.

Data Availability Statement

All the data are reported in the main manuscript and in Supporting Information.

Keywords: 2D-layered materials · CO_2 photoreduction · Exfoliation · g-C_3N_4 · Photocatalysis · Ultrasound

[1] M. I. Alam, R. Cheula, G. Moroni, L. Nardi, M. Maestri, *Catal. Sci. Technol.* **2021**, *11*, 6601–6629.
[2] X. Li, J. Yu, M. Jaroniec, X. Chen, *Chem. Rev.* **2019**, *119*, 3962–4179.
[3] D. Mellmann, P. Sponholz, H. Junge, M. Beller, *Chem. Soc. Rev.* **2016**, *45*, 3954–3988.
[4] B. Loges, A. Boddien, H. Junge, M. Beller, *Angew. Chem. Int. Ed.* **2008**, *47*, 3962–3965.
[5] C. Guo, W. Zhou, X. Lan, Y. Wang, T. Li, S. Han, Y. Yu, B. Zhang, *J. Am. Chem. Soc.* **2022**, *144*, 16006–16011.
[6] B. Shan, S. Vanka, T. T. Li, L. Troian-Gautier, M. K. Brennaman, Z. Mi, T. J. Meyer, *Nat. Energy* **2019**, *4*, 290–299.
[7] W. Reutemann, H. Kieczka, in *Ullmann's Encyclopedia of Industrial Chemistry*, Wiley-VCH , Weinheim **2000**, https://doi.org/10.1002/14356007.a12_013.
[8] ChemAnalyst, https://urldefense.com/v3/__https:/www.chemanalyst.com/industry-report/formic-acid-market-688__!!N11eV2iwtfs!vZ-TDk2gKJlDG2-q3T0R2ldQoB4dXo8TJfVdoCqhb4WAoIGwK3HV_HiZvnYmH4S8xG8UeNzeqv1fF2_7k6W0Ct2Sqg$, https://www.chemanalyst.com/industry-report/formic-acid-market-688 (accessed: December 2024).
[9] IEA, https://urldefense.com/v3/__https:/www.iea.org/reports/global-energy-review-co2-emissions-in-2021-2__;!!N11eV2iwtfs!vZ-TDk2gKJlDG2-q3T0R2ldQoB4dXo8TJfVdoCqhb4WAoIGwK3HV_HiZvnYmH4S8xG8UeNzeqv1fF2_7k6U8DWxxKg$, https://www.iea.org/reports/global-energy-review-co2-emissions-in-2021-2 (accessed: December 2024).
[10] M. F. Philips, G.-J. M. Gruter, M. T. M. Koper, K. J. P. Schouten, *ACS Sustain. Chem. Eng.* **2020**, *8*, 15430–15444.
[11] L. Krishfield, D. Masand, K. Takatsuji, H. Havel, R. Daliah, C. Gee, K. Marshall, Y.-S. Yu, https://luxresearchinc.com/wp-content/uploads/2022/07/lux-research-co2-capture-utliziation-the-emergence-of-a-carbon-economy-executive-summary.pdf (accessed: December 2024).
[12] M. Peplow, *Nature* **2022**, *603*, 780–783.
[13] J. Klankermayer, S. Wesselbaum, K. Beydoun, W. Leitner, *Angew. Chem. Int. Ed.* **2016**, *55*, 7296–7343.
[14] T. Schaub, R. A. Paciello, *Angew. Chem. Int. Ed.* **2011**, *50*, 7278–7282.
[15] A. Weilhard, S. P. Argent, V. Sans, *Nat. Commun.* **2021**, *12*, 1–7.
[16] Y. Tian, Y. Zhou, Y. Zong, J. Li, N. Yang, M. Zhang, Z. Guo, H. Song, *ACS Appl. Mater. Inter.* **2020**, *12*, 34795–34805.
[17] R. Kuriki, K. Sekizawa, O. Ishitani, K. Maeda, *Angew. Chem. Int. Ed.* **2015**, *54*, 2406–2409.
[18] R. Kuriki, O. Ishitani, K. Maeda, *ACS Appl. Mater. Inter.* **2016**, *8*, 6011–6018.
[19] B. Zhou, J. Song, C. Xie, C. Chen, Q. Qian, B. M.o-B.i-C.d T. M. C. Han: *ACS Sustain. Chem. Eng.* **2018**, *6*, 5754–5759.
[20] K. Mori, J. Matsuo, Y. Kondo, H. Hata, H. Yamashita, *ACS Appl. Energy Mater.* **2021**, *4* 11634–11642.
[21] D. Yadav, A. Kumar, J. Y. Kim, N. J. Park, J. O. Baeg, *J. Mater. Chem. A* **2021**, *9*, 9573–9580.
[22] L. Guan, X. Chen, *ACS Appl. Energy Mater.* **2018**, *1* 4313–4320.
[23] J. Wang, R. T. Guo, Z. X. Bi, X. Chen, X. Hu, W. G. Pan, *Nanoscale* **2022**, *14*, 11512–11528.
[24] S. Chen, S. Li, L. Xiong, G. Wang, *Chem. Phys. Lett.* **2018**, *706*, 68–75.
[25] H. Lin, Y. Liu, Z. Wang, L. Ling, H. Huang, Q. Li, L. Cheng, Y. Li, J. Zhou, K. Wu, J. Zhang, T. Zhou, *Angew. Chem. Int. Ed.* **2022**, *61*, e202214142.
[26] X. Wang, S. Blechert, M. Antonietti, *ACS Catal.* **2012**, *2* 1596–1606.
[27] A. Thomas, A. Fischer, F. Goettmann, M. Antonietti, J. O. Müller, R. Schlögl, J. M. Carlsson, *J. Mater. Chem.* **2008**, *18*, 4893.
[28] X. Wang, K. Maeda, A. Thomas, K. Takanabe, G. Xin, J. M. Carlsson, K. Domen, M. Antonietti, *Nat. Mater.* **2009**, *8*, 76–80.
[29] A. Kumar, P. Raizada, V. Kumar Thakur, V. Saini, A. Aslam Parwaz Khan, N. Singh, P. Singh, *Chem. Eng. Sci.* **2021**, *230*, 116219.
[30] G. Gao, Y. Jiao, E. R. Waclawik, A. Du, *J. Am. Chem. Soc.* **2016**, *138*, 6292–6297.
[31] J. Liu, Y. Liu, N. Liu, Y. Han, X. Zhang, H. Huang, Y. Lifshitz, S. Lee, J. Zhong, Z. Kang, *Science* **2015**, *347*, 970–974.
[32] Q. Lin, L. Li, S. Liang, M. Liu, J. Bi, L. Wu, *Appl. Catal. B Environ.* **2015**, *163*, 135–142.
[33] H. Li, H. Tian, X. Wang, M. Pi, S. Wei, H. Zhu, D. Zhang, S. Chen, *ACS Appl. Energy Mater.* **2019**, *2*, 4692–4699.
[34] F. Wang, S. Chen, J. Wu, W. Xiang, L. Duan, *Ind. Eng. Chem. Res.* **2023**, *62*, 15907–15918.
[35] M. J. Lima, A. M. T. Silva, C. G. Silva, J. L. Faria, *J. Catal.* **2017**, *353*, 44–53.
[36] M. F. Vega, C. Olivas, E. Díaz-Faes, C. Barriocanal, *Catal. Today* **2024**, *427*, 114412.
[37] M. Zhang, Y. Yang, X. An, J. Zhao, Y. Bao, L. Hou, *J. Hazard. Mater.* **2022**, *424*, 127424.
[38] J. Xu, L. Zhang, R. Shi, Y. Zhu, *J. Mater. Chem. A* **2013**, *1*, 14766.

[39] I. Papailias, N. Todorova, T. Giannakopoulou, N. Ioannidis, N. Boukos, C. P. Athanasekou, D. Dimotikali, C. Trapalis, *Appl. Catal. B Environ.* **2018**, *239*, 16–26.
[40] A. Beyhaqi, S. M. T. Azimi, Z. Chen, C. Hu, Q. Zeng, *Int. J. Hydrogen Energy* **2021**, *46*, 20547–20559.
[41] M. Telkhozhayeva, E. Teblum, R. Konar, O. Girshevitz, I. Perelshtein, H. Aviv, Y. R. Tischler, G. D. Nessim, *Langmuir* **2021**, *37*, 4504–4514.
[42] Y. Huang, Y.-H. Pan, R. Yang, L.-H. Bao, L. Meng, H.-L. Luo, Y.-Q. Cai, G.-D. Liu, W.-J. Zhao, Z. Zhou, L.-M. Wu, Z.-L. Zhu, M. Huang, L.-W. L. Liu, L.-W. L. Liu, P. Cheng, K.-H. Wu, S.-B. Tian, C.-Z. Gu, Y.-G. Shi, Y.-F. Guo, Z. G. Cheng, J.-P. Hu, L. Zhao, G.-H. Yang, E. Sutter, P. Sutter, Y.-L. Wang, W. Ji, X.-J. Zhou, H.-J. Gao, *Nat. Commun.* **2020**, *11*, 2453.
[43] M. Ahmed, M. A. Akram, A. Bano, M. Z. Khan, R. Rehman, R. Jan, S. A. K. Javed, *Heliyon* **2024**, *10*, e29417.
[44] J. Kim, S. Kwon, D.-H. Cho, B. Kang, H. Kwon, Y. Kim, S. O. Park, G. Y. Jung, E. Shin, W.-G. Kim, H. Lee, G. H. Ryu, M. Choi, T. H. Kim, J. Oh, S. Park, S. K. Kwak, S. W. Yoon, D. Byun, Z. Lee, C. Lee, *Nat. Commun.* **2015**, *6*, 8294.
[45] M. Compagnoni, G. Ramis, F. S. Freyria, M. Armandi, B. Bonelli, I. Rossetti, *Rend. Lincei* **2017**, *28*, 151–158.
[46] F. Conte, A. Villa, L. Prati, C. Pirola, S. Bennici, G. Ramis, I. Rossetti, *Ind. Eng. Chem. Res.* **2022**, *61*, 2963–2972.
[47] F. Galli, M. Compagnoni, D. Vitali, C. Pirola, C. L. Bianchi, A. Villa, L. Prati, I. Rossetti, *Appl. Catal. B Environ.* **2017**, *200*, 386–391.
[48] H. Marsh, F. Rodríguez-Reinoso, In *Activated Carbon*, Elsevier, Amsterdam, Netherlands **2006**, pp. 143–242.
[49] T. Wang, B. Daiber, J. M. Frost, S. A. Mann, E. C. Garnett, A. Walsh, B. Ehrler, *Energy Environ. Sci.* **2017**, *10*, 509–515.
[50] M. Bedendi, I. Rossetti, G. Ramis, Design of Photocatalytic Processes for Solar Fuels Production through CO_2 Photoreduction, University of Milan, **2019**.
[51] J. Tauc, R. Grigorovici, A. Vancu, *Phys. Status Solidi* **1966**, *15*, 627–637.
[52] F. Conte, E. I. García-López, G. Marcì, C. L. M. Bianchi, G. Ramis, I. Rossetti, *Catalysts* **2022**, *12*, 1628.
[53] V. M. Gowri, A. Ajith, S. A. John, *Langmuir* **2021**, *37*, 10538–10546.
[54] S. Yang, Y. Gong, J. Zhang, L. Zhan, L. Ma, Z. Fang, R. Vajtai, X. Wang, P. M. Ajayan, *Adv. Mater.* **2013**, *25*, 2452–2456.
[55] P. Niu, L. Zhang, G. Liu, H. M. Cheng, *Adv. Funct. Mater.* **2012**, *22*, 4763–4770.
[56] E. Alwin, M. Zieliński, A. Suchora, I. Gulaczyk, Z. Piskuła, M. Pietrowski, *J. Mater. Sci.* **2022**, *57*, 15705–15721.
[57] P. Molaei, F. Rahimi-Moghadam, *J. Mater. Sci. Mater. Electron.* **2021**, *32*, 19655–19666.
[58] Y. J. Yuan, Z. Shen, S. Wu, Y. Su, L. Pei, Z. Ji, M. Ding, W. Bai, Y. Chen, Z. T. Yu, Z. Zou, *Appl. Catal. B Environ.* **2019**, *246*, 120–128.
[59] B. L. Phoon, C. W. Lai, G. T. Pan, T. C. K. Yang, J. C. Juan, *Nanomaterials* **2021**, *11*, 2041.
[60] Y. Zhang, Q. Pan, G. Chai, M. Liang, G. Dong, Q. Zhang, J. Qiu, *Sci. Rep.* **2013**, *3*, 1–8.
[61] C. Merschjann, S. Tschierlei, T. Tyborski, K. Kailasam, S. Orthmann, D. Hollmann, T. Schedel-Niedrig, A. Thomas, S. Lochbrunner, *Adv. Mater.* **2015**, *27*, 7993–7999.
[62] T. Kashyap, P. J. Boruah, H. Bailung, D. Sanyal, B. Choudhury, *Nanoscale Adv.* **2021**, *3*, 3260–3271.
[63] E. Bahadori, A. Tripodi, A. Villa, C. Pirola, L. Prati, G. Ramis, I. Rossetti, *Catalysts* **2018**, *8*, 430.
[64] M. Tommasi, F. Conte, G. Ramis, I. Rossetti, *DGMK Tagungsbericht*, **2022**, *2022*, 134–151.
[65] R. C. Pawar, S. Kang, H. Han, H. Choi, C. S. Lee, *Catal. Sci. Technol.* **2019**, *9*, 1004–1012.
[66] K. Zhu, W. Wang, A. Meng, M. Zhao, J. Wang, M. Zhao, D. Zhang, Y. Jia, C. Xu, Z. Li, *RSC Adv.* **2015**, *5*, 56239–56243.
[67] G. Li, L. Li, H. Yuan, H. Wang, H. Zeng, J. Shi, *J. Colloid Inter. Sci.* **2017**, *495*, 19–26.
[68] Q. Tang, X. An, J. Zhou, H. Lan, H. Liu, J. Qu, *J. Colloid Inter. Sci.* **2020**, *579*, 455–462.
[69] W. Liu, T. Yanase, N. Iwasa, H. Koizumi, S. Mukai, S. Iwamura, T. Nagahama, T. Shimada, *Int. J. Hydrogen Energy* **2020**, *45*, 8444–8455.
[70] X. Cai, Z. Jiang, X. Zhang, X. Zhang, *Nanoscale Res. Lett.* **2018**, *13*, 241.
[71] A. V. Tyurnina, I. Tzanakis, J. Morton, J. Mi, K. Porfyrakis, B. M. Maciejewska, N. Grobert, D. G. Eskin, *Carbon* **2020**, *168*, 737–747.
[72] N. S. Taghavi, R. Afzalzadeh, *Arch. Acoust.* **2021**, *46*, 31–40.
[73] Y. Hernandez, M. Lotya, D. Rickard, S. D. Bergin, J. N. Coleman, *Langmuir* **2010**, *26*, 3208–3213.
[74] Z. Li, R. J. Young, C. Backes, W. Zhao, X. Zhang, A. A. Zhukov, E. Tillotson, A. P. Conlan, F. Ding, S. J. Haigh, K. S. Novoselov, J. N. Coleman, *ACS Nano* **2020**, *14*, 10976–10985.
[75] Q. Zhu, Z. Xu, B. Qiu, M. Xing, J. Zhang, *Small* **2021**, *17*, 1–25.
[76] C. Backes, D. Campi, B. M. Szydlowska, K. Synnatschke, E. Ojala, F. Rashvand, A. Harvey, A. Griffin, Z. Sofer, N. Marzari, J. N. Coleman, D. D. O'Regan, *ACS Nano* **2019**, *31*, 7050–7061, https://doi.org/10.1021/acsnano.9b02234.
[77] L. J. Ji, Y. Qin, D. Gui, W. Li, Y. Li, X. Li, P. Lu, *Chem. Mater.* **2018**, *30*, 8732–8738.
[78] P. Niu, Y. Yang, J. C. Yu, G. Liu, H. M. Cheng, *Chem. Commun.* **2014**, *50*, 10837.
[79] G. Dong, L. Zhang, *J. Mater. Chem.* **2012**, *22* 1160–1166.
[80] Y.-P. Yuan, S.-W. Cao, Y.-S. Liao, L.-S. Yin, C. Xue, *Appl. Catal. B Environ.* **2013**, *140–141*, 164–168.
[81] K. Maeda, K. Sekizawa, O. Ishitani, *Chem. Commun.* **2013**, *49* 10127.
[82] J.-C. Wang, H.-C. Yao, Z.-Y. Fan, L. Zhang, J.-S. Wang, S.-Q. Zang, Z.-J. Li, *ACS Appl. Mater. Inter.* **2016**, *8*, 3765–3775.
[83] W.-J. Ong, L.-L. Tan, S.-P. Chai, S.-T. Yong, *Dalt. Trans.* **2015**, *44*, 1249–1257.
[84] J. Yu, K. Wang, W. Xiao, B. Cheng, *Phys. Chem. Chem. Phys.* **2014**, *16*, 11492.
[85] W. Yu, D. Xu, T. Peng, *J. Mater. Chem. A* **2015**, *3*, 19936–19947.
[86] Y. He, L. Zhang, M. Fan, X. Wang, M. L. Walbridge, Q. Nong, Y. Wu, L. Z., Zhao , *Sol. Energy Mater. Sol. Cells* **2015**, *137*, 175–184.
[87] K. Maeda, G. Sahara, M. Eguchi, O. Ishitani, *ACS Catal.* **2015**, *5*, 1700–1707.
[88] D. O. Adekoya, M. Tahir, N. A. S. Amin, *J. CO_2 Util.* **2017**, *18*, 261–274.
[89] L. Yang, R. P. Sivasankaran, M. K. Song, A. U. Pawar, D. K. Lee, Y. S. Kang, *Adv. Energy Mater.* **2025**, *15*, 202402798.
[90] F. Yu, L. Chen, X. Shen, X. Li, C. Duan, *APL Mater.* **2019**, *7*, 101101.
[91] M. Liang, T. Borjigin, Y. Zhang, B. Liu, H. Liu, H. Guo, *Appl. Catal. B Environ.* **2019**, *243*, 566–575.
[92] M. Li, L. Zhang, X. Fan, M. Wu, M. Wang, R. Cheng, L. Zhang, H. Yao, J. Shi, *Appl. Catal. B Environ.* **2017**, *201*, 629–635.
[93] S. Huang, Y. Long, S. Ruan, Y.-J. Zeng, *ACS Omega* **2019**, *4*, 15593–15599.

Manuscript received: December 28, 2024
Revised manuscript received: May 4, 2025
Accepted manuscript online: May 23, 2025
Version of record online: ■■, ■■